The mechanics of a magma chamber-fault system in trans-tension with application to Coso

Alexander G. Simakin, Ahmad Ghassemi*

Department of Petroleum Engineering, Texas A&M University, College Station, TX 77843, USA

Abstract

The mechanical interaction between an elliptically shaped magma chamber and a fault subject to transtension is investigated with particular reference to the Coso geothermal field. The geologic setting of the Coso field is interpreted as a releasing bend step-over structure formed by the Airport Lake and Owens Valley dextral strike-slip fault system. The role of the Coso volcano-magmatic center in the development of the "over-step" structure is examined by treating the magma chamber as a liquid inclusion in a viscoelastic crust containing a fault (Airport Lake). The problem is numerically solved using a 2D viscoelastic finite element model with thermally activated viscosity to account for thermal weakening of the rock. The temperature distribution around the magma body is calculated based on a 3D steady-state approach and using the mesh-less numerical method. The fault is modeled as a frictionless contact. The simulated distributions of stress and strain around the inclusion display a rotation caused by the shearing component of the applied transtension. The results indicate that the fault tends to overstep the chamber in a geometric pattern similar to a step-over. There is good correspondence between the computed distributions of the maximum shear stress in the vicinity of the magma chamber and the map of earthquake epicenters at a depth of 7–10 km in Coso.
© 2007 Elsevier Ltd. All rights reserved.

Keywords: Coso; Inclusion; Magma chamber; Stepover; Transtension; Thermally activated viscosity; Viscoelasticity; Strain weakening

1. Introduction

Large rheological inhomogeneities (on the continental, regional and local scales) can have a significant impact on the stress distribution in the crust. Magma bodies in the crust can be viewed as inclusions that interact with the tectonic deformation leading to stress/strain concentrations and large stress gradients and rotations.

Analogue modeling confirms such coupling to be important in rift zones, where the resulting strain localization forms a graben above the magma chamber causing further magma emplacement and regulating the geologic structure in the extensional environment (Corti et al., 2003). There are geologic arguments supporting close association between shear zones and granite plutons (Weinberg et al., 2004).

This paper examines the interaction between a magma body and a fault in transtension, focusing on the impact of the chamber on the behavior of a strike-slip fault. The occurrence of a fault-magma chamber system is related to circumstances dictated by the large scale processes in the mantle which often place volcanic centers on the propagation path of major faults. The Coso geothermal field (SE California) represents such a situation. The current deformation in Coso is well studied by modern geodetic methods (GPS and InSAR). High seismic activity around Coso Range is suggestive of its internal structure. Using this data, Unruh et al. (2001) have estimated the position of a magma body and the orientation and magnitude of the stresses in the Coso area. Herein a numerical model is used to study the fault/magma chamber interaction to provide additional insights regarding the dynamics of the Coso geothermal field and its interpretation.

* Corresponding author. Tel.: +1 979 845 2206; fax: +1 979 862 6579.
E-mail address: ahmad.ghassemi@pe.tamu.edu (A. Ghassemi).

1.1. The geological setting and seismicity of the Coso volcano-magmatic center

The Coso geothermal field is hosted by a magmatic center that had been active since Pliocene until historical time. The last rhyolite domes (Sugar Loaf Mt. and others) are dated ca. 39,000 yrs (Manley and Bacon, 2000). The most recent volcanic activity at Red Hill (North of the Coso Range) is dated at about 10,000 yrs. There are signs that geothermal activity has recently increased; the modern geothermal system reflects renewed magmatic activity beneath the Coso dome field as indicated by temperatures that exceed 325 °C, and high ^{3}He/^{4}He ratios (Welhan et al., 1988).

Broadly speaking, the Coso Range is located between the Sierra-Nevada microplate and the Basin and Range extensional zone (see Fig. 1). The tectonic setting is determined by the interaction between the western margin of North America plate and the relatively rigid Pacific plate, so that shear is distributed in a system of strike-slip faults in a zone that

extends hundreds of kilometers eastward (Miller et al., 2001). The Owens Valley, with Coso Range at its southern end, is one of the large structural basins north of the Garlock fault, where dextral shear strains are concentrated. The azimuth of the cumulative relative motion lies counterclockwise from the strike of the local faults resulting in a transtensional environment.

More specifically, InSAR observations (Peltzer et al., 2001) have pointed out that the Garlock (left lateral–sinistral) and Blackwater–Little Lake (dextral) faults are intersecting conjugate strike-slip faults. The quadruple junction that they form is kinematically unstable and may generate an oscillatory surface-velocity pattern in which faults would localize shear strain one at a time. InSAR observations suggest that strain is accumulated along the Blackwater–Little Lake fault system with the Garlock fault presently inactive. These faults intersect in the direction of the Owens valley–Airport Lake pair.

Seismic data have provided insight into the deep structure of the Coso area; Hauksson and Unruh (2003) inverted P
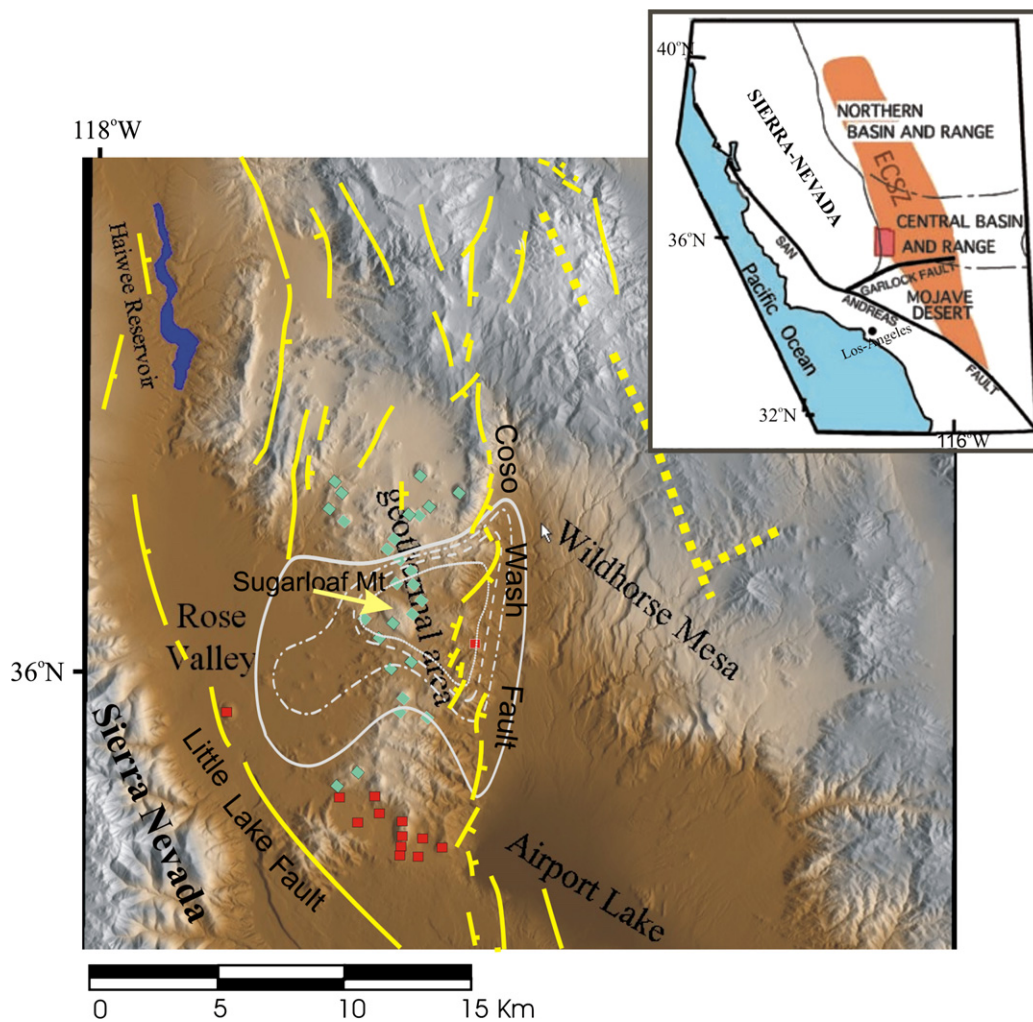

Fig. 1. A schematic geologic map of the Coso area. Red lines are contours of the heat flux from Combs (1980) (values: 3, 5, 10, 15 HFU). Yellow lines depict the positions of faults (from Unruh et al., 2003). Blue diamonds denote rhyolitic vents younger than 0.3 Ma; red squares denote basaltic vents younger than 0.3 Ma (from Wicks et al., 2001). The general position of the Coso geothermal area in the East California Shear Zone (ECSZ) is indicated by the red rectangle in the inset (modified by the permission of American Geophysical Union). 1 HFU = 41.87 mW/m^2.

and $S–P$ arrival times from 11,500 earthquakes to determine the 3D V_p and V_p/V_s velocity structures to depths of 20 km. They found a low V_p/V_s zone at a depth of 6–9 km under the geothermal field capped by a cloud of earthquake epicenters. This structure might be interpreted as a partially solidified magma that provides a large heat flux that drives the surface geothermal activity. The presence of a high fraction of fluid is plausible in view of low V_p/V_s (Patane et al., 2006). Heating of silicic magma with fresh basaltic influx is necessarily accompanied by basalt crystallization and release of CO_2–H_2O and thus, possible fluid accumulation. Alternatively, relatively a large fluid fraction could be due simply to magmatic mash solidification with fluid exsolution and accumulation.

Unruh et al. (2001) used a new seismic imaging method and 2D acoustic velocity tomograms to determine the detailed structure of the geothermal area and its surroundings. They found the trace of Coso Wash fault bounds the eastern margin of the geothermal field. Some SE dipping structures (probably active faults) are also detected. All faults tend to flatten as they terminate at a depth of about 4 km. This is thought to correspond to a decollement at the brittle–ductile transition depth. Also, a strong reflector has been found at a depth of 6 km that might represent the top of the magma chamber or a deep fractured geothermal reservoir.

Feng and Lees (1998) performed focal mechanism and stress analysis of the microseismisity in Coso. They detected that the major principal stress, S_1, rotates from horizontal to almost vertical in a zone around the geothermal production area. The field has a fast subsidence rate which might have a poroelastic nature related to steam production and rapid cooling of the reservoir that would theoretically produce a uniform plane extension (constricted contraction), and rotate the σ_1-direction.

Altogether the data cited suggest the magmato–tectonic interaction to be significant in deformation and geothermal activity of the Coso area, and we illustrate certain mechanical aspects of this coupling herein. Using numerical simulations, the interactions between the magma chamber and a fault are examined in relation to the fundamental features observed in Coso. In order to facilitate the analysis of the problem, we first use the analytical solution to the simple model of a 2D circular inclusion in a viscoelastic matrix to find the influence of the magma chamber on the stress and displacement distributions in the crust. The stress distribution for the more realistic elliptical geometry which is generally used to model magma chambers is topologically similar to the circular one.

2. Analytic solutions for weak inclusions in a deforming solid

2.1. Circular hole in an elastic material

Influx of fresh magma or fluid release can over-pressurized a magma chamber and result in surface uplift. On the other hand, under pressure due to cooling-induced contraction, crystallization and escape of the released fluid cause subsidence above the underpressurized chamber. The case of an under-pressurized magma chamber (pressure lower than mean stress in the host rock) in an elastic crust subjected to tension can be viewed and treated as a hole in an elastic infinite plate. The solution to this problem can be found in terms of complex potentials using Muskhelishvili's method of Complex Variables theory (see e.g., in Savin, 1970). The governing equations of the problem are the mechanical equations of equilibrium (tension is considered positive):

$$\frac{\partial \sigma_{xx}}{\partial x} + \frac{\partial \sigma_{xy}}{\partial y} = 0, \ \frac{\partial \sigma_{yy}}{\partial y} + \frac{\partial \sigma_{yx}}{\partial x} = 0 \tag{1}$$

and the stress compatibility condition (obtained using the stress–strain relationship):

$$\left(\frac{\partial^2}{\partial x^2} + \frac{\partial^2}{\partial y^2}\right)(\sigma_{xx} + \sigma_{yy}) = 0 \tag{2}$$

The above equations result in the biharmonic equation in terms of the Airy's stress function, $U(x, y)$:

$$\frac{\partial^4 U}{\partial x^4} + 2\frac{\partial^4 U}{\partial x^2 \partial y^2} + \frac{\partial^4 U}{\partial y^4} = 0 \tag{3}$$

Then, the stresses are written in terms of the derivates of $U(x, y)$ as:

$$\sigma_{xx} = \partial^2 U/\partial y^2, \ \sigma_{xy} = -\partial^2 U/\partial x\, \partial y, \ \sigma_{yy} = \partial^2 U/\partial x^2 \tag{4}$$

The stress function, $U(x, y)$, can be expressed in terms of two analytical functions $\phi(z)$ and $\chi(z)$ as:

$$U(x,y) = \mathrm{Re}(\overline{z}\phi(z) + \chi(z)) \tag{5}$$

The functions $\phi(z)$ and $\chi(z)$ are chosen to satisfy the problem boundary conditions. The stresses and displacements (u_x, u_y) are expressed as follows:

$$\begin{aligned}
(\sigma_{xx} + \sigma_{yy})/2 &= 2\,\mathrm{Re}(\phi'(z)) \\
(\sigma_{yy} - \sigma_{xx})/2 + is_{xy} &= \overline{z}\phi''(z) + \chi'(z) \\
u_x + iu_y &= \frac{(3-4\nu)\phi(z) - \overline{Z\phi'(z)} - \overline{\chi}(z)}{2\mu}
\end{aligned} \tag{6}$$

where ν is the Poisson's ratio. The complex potentials for a circular hole of radius r_c in a *compressible elastic solid* (plane strain) subjected to uniaxial tension ($\sigma_{xx} = p$) can be found in Savin (1970) for the case when the hole boundary is stress free (empty hole):

$$\begin{aligned}
\phi(z) &= \frac{pr_c}{4}\left(\frac{z}{r_c} + \frac{2r_c}{z}\right) \\
\chi'(z) &= -\frac{pr_c}{4}\left(\frac{z}{r_c} + \frac{r_c}{z} - \left(\frac{r_c}{z}\right)^2\right)
\end{aligned} \tag{7}$$

These functions yield simple closed-form expressions for the stress components in the polar coordinates (r, θ), where

r is the radial distance and θ is the angle measured counter-clockwise from the *x*-axis:

$$\sigma_{rr} = \frac{p}{2}\Big[(1-\rho^2) + (1-4\rho^2+3\rho^4)\cos2\theta\Big]$$

$$\sigma_{\theta\theta} = \frac{p}{2}\Big[(1+\rho^2) - (1+3\rho^4)\cos2\theta\Big] \qquad (8)$$

$$\tau_{\theta r} = \frac{p}{2}(1+2\rho^2-3\rho^4)\sin2\theta$$

where $\rho = r_c/r$. As shown in Fig. 2, the differential stress distribution computed using Eq. (8) has a butterfly pattern, with two symmetry axes and zones of shear stress minima that are oriented parallel to the applied extension direction.

2.2. Incompressible medium, simple and pure shear

The viscous limit can be used to calculate the long-term differential stress distribution for a Maxwell material. Formally, the constitutive equations for an incompressible viscous matrix are the same (by substituting strain rate for strain) as those for an incompressible elastic body. For *an incompressible viscous matrix*: $\sigma + \mathrm{PI} = 2\eta D$, where D is rate of strain tensor $D_{ij} = 1/2((\partial u_i/\partial x_j) + (\partial u_j/\partial x_i))$. For an *incompressible elastic body*: $\sigma + \mathrm{PI} = 2\mu e$ which follows from the general equation $\sigma - \lambda I e_{kk} = 2Ge_{ij}$ with $\nu = 0.5$, where λ and μ are Lame parameters. As a result therefore, when $\nu = 0.5$ (incompressible elastic solid) Savin's solution (Eq. (6)) describes the problem of a hole in an incompressible viscous matrix subjected to extension. Muskhelishvili's method can be used to treat the problem of incompressible liquid in a hole which approximates a filled magma chamber. It should be noted that here the magma pressure is defined by mechanics of deformation and not by any influx of fresh magma or other physical processes.

For a general shear loading, the complex potentials for the problem of an incompressible viscous inclusion in an incompressible viscous matrix are (Schmid and Podladchikov, 2003):

$$\phi(z) = -\frac{i}{2}\eta_m\dot\gamma z - (i\dot\gamma+2\dot\varepsilon)Ar_c^2z^{-1}$$

$$\chi(z) = (i\dot\gamma-2\dot\varepsilon)\eta_m z - (i\dot\gamma-2\dot\varepsilon)Ar_c^4z^{-3}, \ A = \frac{\eta_m(\eta_c-\eta_m)}{\eta_c+\eta_m} \qquad (9)$$

where η_m is the matrix viscosity and η_c is inclusion viscosity, $\dot\gamma$ and $\dot\varepsilon$ are simple and pure shear rates, respectively. We consider the case of a weak inclusion, i.e., when the matrix viscosity is much greater than the viscosity of the inclusion $\eta_m \gg \eta_c$. This is a reasonable assumption as the viscosity of melt is indeed of the order 10^5–10^{10} Pa s which is much less than the viscosity of the surrounding rocks (10^{16}–10^{22} Pa s). In this case, $A = -\eta_m$ and the velocity field does not depend on the rheology of the system. After substituting Eq. (8) into Eq. (5), the expressions for the stress components, flow velocities and principal stresses can be derived. For example, the mean stress for simple shear (at $r > r_c$ and $0 < \theta < 2\pi$, $\bar r = r/r_c$) is:

$$P = \frac{4\dot\gamma\eta_m\sin2\theta}{\bar r^2} \qquad (10)$$

And the flow rates are:

$$V_y = -\frac{\dot\gamma r_c\cos\theta}{2}\left[4\cos^2\theta\left(\frac{1}{\bar r}-\frac{1}{\bar r^3}\right)+\frac{3}{\bar r^3}-\frac{4}{\bar r}\right]$$

$$V_x = \frac{\dot\gamma r_c\sin\theta}{2}\left[4\cos^2\theta\left(\frac{1}{\bar r}-\frac{1}{\bar r^3}\right)+\frac{1}{\bar r^3}+2\bar r\right] \qquad (11)$$

$(S_1 - S_2)$ can be expressed as a function of 4θ, implying a periodicity of $\pi/2$, and a cross pattern:

$$S_1 - S_2 = \frac{2\dot\gamma\eta_m}{\bar r^4}\sqrt{(3-2\bar r^2)^2+\bar r^4(\bar r^4+\cos4\theta(4\bar r^2-6))} \qquad (12)$$

The distribution of flow lines indicates strain localization, and stress concentration around the inclusion. As can be seen in the Fig. 2, there are four $(S_1 - S_2)$ maxima located on the boundary of the inclusion with magnitudes twice that of the far field value. The zones of high $(S_1 - S_2)$ concentration extend into the matrix as illustrated by the four narrow radial zones. Four shear stress maxima are located inside these strips. The largest value of each strip (1.33 times the value at infinity) occur a distance equal to 0.73 times the radius of the inclusion away from the boundary.

The above solution corresponds to the case of simple shear. The results of simple and pure shear loadings are the same for *incompressible* materials in the sense that in both cases the normalized principal strains are $(\pm1, \pm1)$ with a zero trace. In other words, the displacement field for one can be used to obtain the strain rate tensor of the other by rotating the coordinate system. Specifically, the deviatoric part of the strain rate tensor for the case of pure shear can be transformed into simple shear by rotating the coordinate system through $\pi/4$. It follows that the cross formed by the lines connecting the points of maximum shear stress in *pure shear* ($\dot\gamma = 0$, or axial tension or compression), is rotated by $\pi/4$ relative to its position for *simple shear*, and becomes diagonal. For mixed shear loading, the cross for the maximum shear around the inclusion will be in an intermediate position between the ones for simple and pure shear cases.

$$S_{pure} = \begin{vmatrix} 1 & 0 \\ 0 & -1 \end{vmatrix}, \ S_{simple} = \begin{vmatrix} 0 & 1 \\ 1 & 0 \end{vmatrix},$$

$$S_{simple} = R\cdot S_{pure}\cdot R^{-1}\big|_{\theta=\pi/4}, \quad R = \begin{vmatrix} \cos\theta & \sin\theta \\ -\sin\theta & \cos\theta \end{vmatrix}$$

As shown in Fig. 2, the cross pattern is modified into a butterfly pattern with a pair of maximum shear zones merging to form "wings" for the case of a hole in a *compressible elastic* material. This pattern has two axes of symmetry with zones of shear stress minima oriented parallel to the extension direction.

The conclusions of above fundamental analysis can be summarized as follows:

(i) *An under-pressurized chamber* ($P_{magma} - P_{lithostatic} < 0$) that develops due to internal processes such as
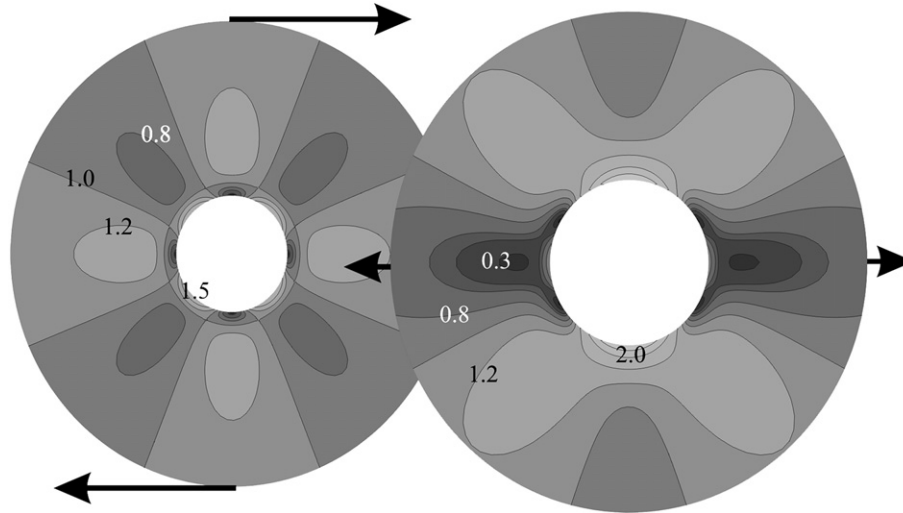
Fig. 2. Cross and butterfly patterns corresponding to distributions of $(S_1 - S_2)$ around an incompressible liquid inclusion in infinite space in simple shear, and a hole in an infinite plate subjected to pure shear, respectively (numbers are values of stress, normalized by the deviatoric stress and σ_{xx} at infinity for each case, respectively).

contraction and fluid loss, or cavity volume enlargement caused by deformation, behaves like an empty hole and results in a "butterfly" $(S_1 - S_2)$ pattern.

(ii) *An over-pressurized chamber* $(P_{\text{magma}} - P_{\text{lithostatic}} \geq 0)$ in shear results in a cross-like $(S_1 - S_2)$ pattern; same as that observed in the uncompressible limit.

Additional factors such as the influence of the complex rheologies and boundary conditions on the solution deserve a numerical study. We perform two series of numerical experiments. In the first series the general situation of an elliptical liquid inclusion in a viscoelastic plate subject to transtension is simulated. The results show that the pattern of the maximum shear stress distribution transitions from the cross-like pattern to a more complex distribution in the course of deformation, and the liquid pressure drops. In the second series of experiments we include kinematics and the effect of temperature on the rock rheology. The simulations are performed by considering a horizontal cross-section at the mid-intrusion level in the Coso geothermal field.

3. Numerical experiments

3.1. Equations and numerical approach

The equations governing the mechanics of the problem include the constitutive equations for the Maxwell solids plus the "equation of state" for the magma (reduced to compressibility for simplicity), and mechanical equilibrium without the gravity term. The equations are solved using the FEM with bilinear elements (Simakin and Ghassemi, 2005) in an unstructured grid that is refined near the chamber boundary and at the fault tip. The fault is viewed as a frictionless contact surface with the non-penetration condition imposed by the penalty

method (Carstensen et al., 1999). No special measure is applied to describe the appropriate stress singularity at the fault tip as fault propagation is not modeled.

The previously discussed analytical solutions have been used to test our FEM code. Comparison of the $(S_1 - S_2)$ values from analytical and numerical solutions demonstrates that the boundaries of the computational domain affect the solution. Comparison of the numerical and analytical values of $(S_1 - S_2)$ on the chamber boundary indicates a mean difference in the range of 5–15%. This is due to the use of about 1300 bilinear elements and can be mitigated using other element types or by mesh refinement, however, bilinear elements are appropriate when modeling more complex nonlinear systems with viscoelastic rheology and viscous damage accumulation and healing under thermal perturbations.

3.2. Rheology: temperature dependence and structural viscosity

The rocks surrounding the magma chamber are treated as a Maxwell solid with a temperature dependent viscosity. Experimental strain–stress relations are usually represented as (Stockhert et al., 1999):

$$\dot{\varepsilon} = H \exp(-Q/RT)\sigma^n \qquad (13)$$

For typical strain rates of 10^{-13}–10^{-14} s^{-1}, the apparent viscosity can be expressed as:

$$\eta = b\exp(Q/nRT), \quad b = H^{-1/n}\dot{e}^{-1+1/n} \qquad (14)$$

As an example, we use experimental data and calculate quartzite viscosities as a function of temperature at a strain rate of 10^{-14} s^{-1}. To bracket possible viscosity variations, we use stiffer (Koch et al., 1989) and softer (Jaoul et al., 1984) wet quartzite rheologies (viscosity 1: $\log(H) = -5.94$

[MPa^{-n}/s], $n = 1.7$, $Q = 134$ [KJ/mol] and viscosity 2: log $(H) = -2.54$, $n = 1.8$, $Q = 151$). At a temperature of $T = 750\,°C$ (close to the eutectic point, i.e., where granites begin to melt at $P_{H2O} = 1$ kbar) a viscosity of 8.3×10^{17} Pa s is considered ''weak'', while a value of 8.3×10^{18} Pa s is stiff.

As follows from Eq. (14), viscosity is the power exponent of the strain rate with coefficients that depend on texture. When modeling strain localization, it is possible to take into account the transient nature of the evolution of texture in response to the applied strain rate. This can be done using a dynamic equation for the scalar compliance, C:

$$\frac{dC}{dt} = Bf\left(|\dot{e}|\right) - AC, \; C = \frac{1}{\eta} \tag{15}$$

where $|\dot{e}|$ is $\sqrt{\dot{e}_{ij}\dot{e}_{ij}/2}$. Then, the power law viscosity arises as the asymptote of the evolution equation:

$$\eta_{ss} = \frac{B}{A}|\dot{e}|^{(-1+1/n)} \quad \text{if } f\left(|\dot{e}|\right) = |\dot{e}|^{(1-1/n)} \tag{16}$$

Then, viscosity can be decomposed into temperature and texture dependent terms: $\eta = \eta_1(T)\eta_2(t)$. The temperature dependent term equals the viscosity at a given T and standard strain rate: $\dot{e} = \dot{e}_0 = 10^{-14}$ s^{-1}; and the structural term, $\eta_2(t)$, is strain-rate and time dependent in accordance with Eq. (16). To satisfy Eq. (16) at steady state, coefficients A and B should satisfy the condition: $B/A = \dot{e}_0^m$. The absolute values of kinetic coefficients (A, B) regulate the rate of the structural transformation. However, these coefficients are not experimentally investigated to date and therefore, they are auxiliary to the constants that reflect the temperature effect. One might choose the values of A and B such that they yield a structural factor in the neighborhood of the initial value of unity. If the initial value of the structural term, $\eta_2(0, x, y)$, is much lower than A/B, then the material has experienced healing that is not related to the deformation pattern. As a result we do not consider dynamic power rheology in the numerical simulations of the Coso described herein.

3.3. General elliptical liquid inclusion in a viscoelastic material subjected to transtension

As a first step in considering a geologically more relevant case, a simplified system consisting of an inclusion in a viscoelastic media subjected to transtension (isothermal) is considered. An elliptical inclusion with $(a/b) = 0.4$ is placed in a narrow elongated strip (to minimize end effects) with its minor axis parallel to direction of shear; this orientation maximizes the effect of rotation. Displacement boundary conditions are applied to the sides of the rectangular domain. The left side is assigned a constant velocity in the direction of $20°$ from OX-direction. To simulate the transtensional deformation regime, the displacement rate is assumed to vary linearly with the OY-axis (along the right and left sides). The lower side is fixed, and then a relatively small strain of 1.7% is applied. The melt pressure inside the inclusion is iteratively adjusted to the deformation. The net result is that the

initially rectangular domain extends in the vertical direction and deforms to become a parallelogram. All numerical experiments are carried out with a Deborah number ($De = \eta/\mu t$) < 0.1, where μ is the shear modulus and t is time. For $De \ll 1$, the material behaves as a purely viscous fluid while for $De \gg 1$ it is as an elastic solid. At our time scales transient viscoelastic behavior is expected.

3.3.1. Scaling

All calculations are performed in non-dimensional form using scaled values of length, time, and pressure. Choosing a pressure scale of 350 bar, the Young modulus becomes 35 GPa, the Poisson ratio is taken as $\nu = 0.2$ and liquid compressibility $K_1 = 45$ GPa. The viscosity of the matrix is set to 10^{19} Pa s, so that the time scale is 2.9×10^{10} s or 906 yrs with a strain rate of 6.0×10^{-13} s^{-1}. It should be noted that the linear scale is arbitrary, so the results can also be used to describe a weak inclusion at the mega-scale ($L = 10$ km) or micro-scale ($L = 1$ cm).

For a crustal rock viscosity of 10^{20} Pa s, these same computational results would correspond to a time scale of 9060 years with a strain rate of 6×10^{-14} s^{-1}. In the following, we consider the results for a non-dimensional time of zero (i.e., elastic case) and 1.0 (9060 yrs).

As can be seen in Fig. 3, the initial stress distribution qualitatively corresponds to the analytical solution of Schmid and Podladchikov (2003) for a circular incompressible liquid inclusion. But, the cross-like pattern of the maximum shear stress ($S_1 - S_2$) is now modified due to the elliptic shape of the inclusion. The initial compressive stress was set to 700 bar to equilibrate the initial melt pressure. The mean compressive stress in the material experiencing relative motion towards the inclusion boundary is higher than the material behind it. The deformation of the boundary causes the pressure in the inclusion to drop to zero from its initial non-dimensional value of 2 (700 bar at scale $P_0 = 350$ bar). This occurs at a non-dimensional rate of 3.38 (or 350/906 ≈ 0.4 bars/yr) for a weak crustal viscosity with a fast strain rate (or equivalently at 0.04 bar/yr for stiff rheology and a slower deformation rate). Initially, the filled inclusion deforms as in the solution by Schmid and Podladchikov (2003). Applied extension causes the magma pressure to drop and eventually the inclusion behaves like ''a hole'' (in fact, there is still liquid inside but it does not totally fill the void) as in the solution by Savin (1970). Gradually, the maximum shear deformation around the under-pressurized inclusion develops a spiral pattern. The minimum structural component of viscosity also has a spiral distribution with weak zones approximately following the expected shear fracture orientations. In Fig. 3 arrows depict the directions of the principal extensional strain. The shear stress minimum and the structural viscosity maximum are located along the extensional direction.

3.3.2. Failure criterion

Shear fracturing is controlled by the value of differential stress ($S_1 - S_2$) and the mean effective stress [$(S_1 + S_2)/2$], where S_1 and S_2 are the major and minor principal stress,
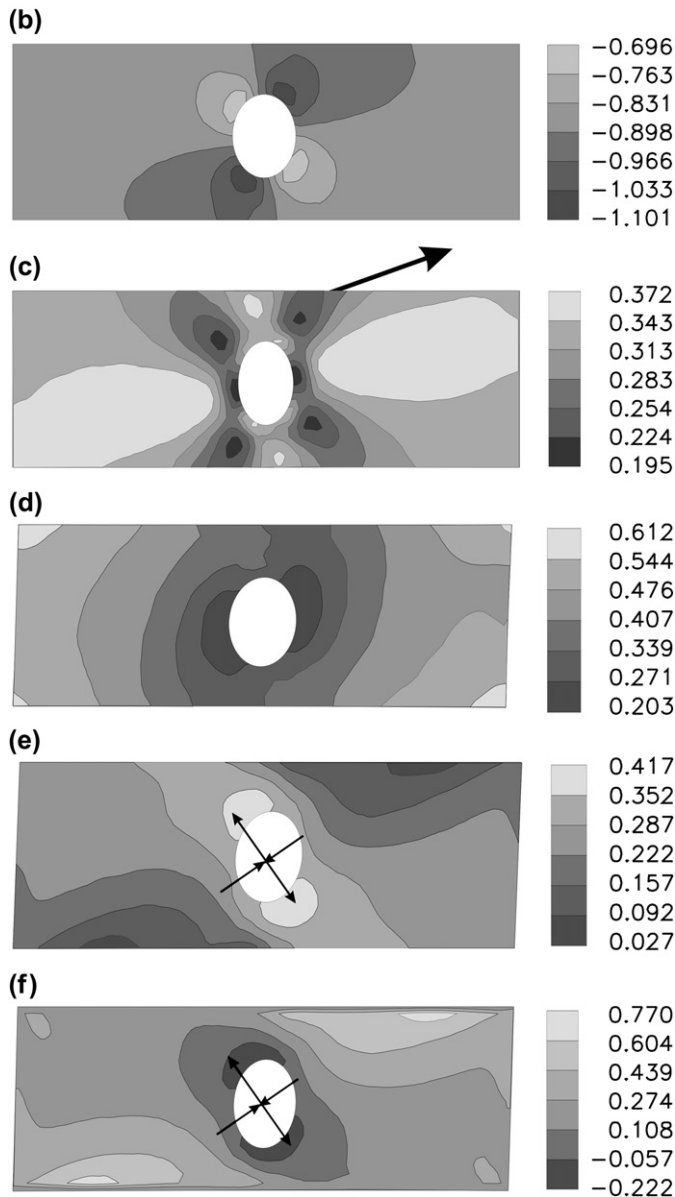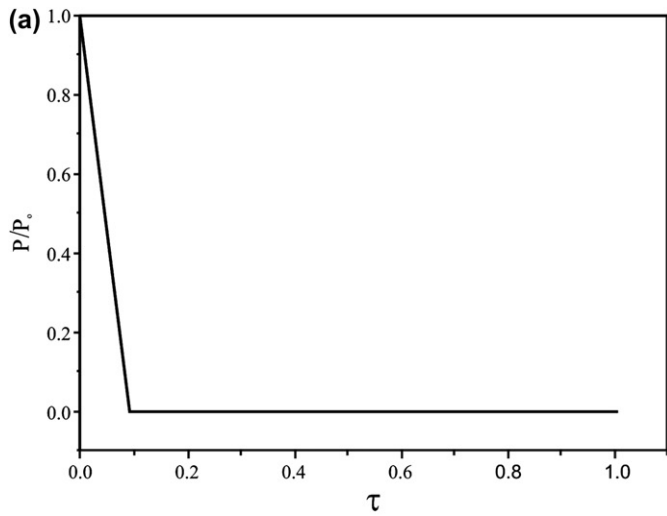
respectively. For example, according to Mohr−Coulomb criterion:

$$\frac{S_1 - S_2}{2} + \left(\frac{S_1 + S_2}{2} + P_{fl}\right)\sin(\phi) = C\cos\phi$$

where ϕ is the friction angle, and C is cohesion. In the current 2D formulation that uses horizontal sections, it is not possible to include gravity load, and the fluid pressure is unknown. This precludes direct use of this failure criterion. However, it can be suggested that at low effective stress (high fluid pressure), the failure distribution will follow a cross or butterfly pattern.

4. Numerical simulations for Coso

In Coso, the magma chamber is located in a zone of transtension or mixed simple and pure shear. The elastic component of the deformation is important as periodic earthquakes lead to cycles of stress accumulation and release. Therefore, one might expect the evolution of the maximum shear stress pattern to fall somewhere between the elastic "butterfly" and the viscous "cross" regimes. The actual structure of the Coso field is rather complicated and merits a 3D treatment. However, for simplicity we reduce the full problem to 2D and consider a representative horizontal section in transtension. As it is not possible to introduce gravity loading in this 2D representation, only information concerning the shear stress is considered, and those features that are related to the horizontal shear strains are captured.

4.1. Calculation of the temperature field

The elevated temperature in the thermal aureole around an intrusion decreases the viscosity and causes relaxation of the effective deviatoric stresses, therefore an estimate of the temperature field is necessary. The real thermal history of

Fig. 3. Numerical experiments for deformation of a rectangular domain with an elliptical inclusion. The velocity vector applied to the top side is inclined 20° from the horizontal (counter-clockwise). The black lines show the principal strains with the long arrow corresponding to the principal extension direction. Results of calculations at the initial elastic stage, $\tau = 0.005$, in (b) and (c); and at the end of the runs, $\tau = 1.0$, for (d−f) with a total strain of $e_{xx} = 1.67\%$. Values of the stresses are normalized by P_0 (e.g. 350 bar, see Section 3.3.1). The time scale depends on the assumed viscosity. (a) Magma pressure variation during numerical simulations, it linearly drops to zero. (b) The mean stress distribution at the onset of deformation. It is similar to mean stress distribution around a hole in an infinite elastic plate in simple shear. (c) Distribution of $(S_1 - S_2)$ at the onset of deformation. It is similar to the cross pattern of the maximum and minimum values around a circular inclusion in a plate (viscous or elastic). (d) Mean stress at the end of the simulation, the spiral pattern develops with viscous relaxation and interaction with the walls of the domain. (e) Distribution of $(S_1 - S_2)$ at the end of deformation. The spiral, "step over"-like pattern can be recognized by $(S_1 - S_2)$ values of on the level of about 0.25, while the maxima of the differential stress are adjacent to the zones lagging behind the rotating inclusion. (f) The structural viscosity distribution (log η_2) reflects the strain-weakening of rocks, with initial value $\eta_2 = 10$, in a "step- over" pattern (arrows show the principal strain directions at infinity beyond the influence of the inclusion).

a magmatic center can be very complex and consists of a sequence of basaltic and rhyolitic magma emplacements. Also, heat due to the decay of radioactive elements, magma crystallization and devolatization contribute to the thermal balance. In view of these complications, a simplified thermal field is used in the mechanical modeling for the purpose of the present work.

In 3D geometry, the temperature field can be characterized by a quasi steady-state distribution assuming that the heat loss towards the surface is compensated by input of fresh magma (in the long term). Using this approach, the temperature distribution for 3D conductive heat transfer (governed by: $\partial T / \partial t = c_T \Delta T$ where c_T is the thermal diffusivity) is obtained using a mesh-less inverse multi-quadric method (IMQ). This method (Cheng et al., 2003) consists of using a global approximation for the temperature, $T(x, y, z)$, that is represented as a sum of probe functions that cover the entire solution domain (as opposed to the FEM where local probe functions have non-zero values only on the local elements). The probe function used is:

$$T(x,y,z) = \sum_N \frac{a_i}{(r - b_i)^2 + c_i^2}$$

where $b_i = (x_i, y_i, z_i)$ are the coordinates of the collocation points distributed in the domain where the solution is sought. The coefficients (a_i) are unknown and need be found such that $T(x, y, z)$ satisfies the required partial differential equation and boundary conditions. For example at a point R, Laplace's equation reads:

$$\Delta T(x,y,z) = \Delta \left(\sum_N \frac{a_i}{(r - b_i)^2 + c_i^2} \right) \Bigg|_{r=R} = 0$$

For n terms in the sum, a set of N points, r_i, are needed to determine the N coefficients, a_i. Each term is applicable in the whole solution domain, therefore, equations for a collocation point m contain all N terms resulting in a dense matrix. A modified version of the meshless method is used in which the variable approximation parameter, c, depends on the collocation point density. The 3D Laplace equation can be solved using the finite element, finite difference or boundary element method, however, the mesh-less approach provides an opportunity to treat geometrically complex problems with relative ease and computational efficiency. The efficiency of the method is, however, somewhat reduced due to a dense matrix that results from the global approximation inherent in the method.

4.2. The simulation domain

The shape and position of the magma chamber in Coso is not known with certainty. The 3D geometry of the mature magma chamber under Coso geothermal field can be reconstructed using the seismic data of Hauksson and Unruh (2003) who present two vertical sections of V_p/V_s ratio delineating the volume of the low seismic velocities and low V_p/V_s ratio (see Fig. 4a). These regions can be attributed to three-

phase mash (melt + minerals + gas) with an increased fluid fraction. Wilson et al. (2003) analyzed seismograms from teleseismic rays crossing the Coso geothermal area, and conclude that V_s shows significant drop (from 2.6 km/s to 1.8 km/s) at a depth around 5 km beneath geothermal center (see Fig. 4b). They link this transition with a shallow magma chamber. However, a lower geothermal reservoir that is not connected with the exploited upper reservoir could be in the roof of a deeper solidifying intrusion. Hager et al. (2003) have analyzed the seismic and postseismic deformations during the quake of July 17, 2001 (California–Nevada border region, Coso, Mw = 5.2). They concluded that a dislocation in a uniform elastic half-space does not explain ''coseismic'' displacements, and that the observed viscoelastic relaxation implies a magma chamber or some process in the geothermal reservoir.

We approximate the magma chamber as an ellipsoid with its dimensions inferred and estimated from the most comprehensive seismic data and interpretations of Hauksson and Unruh (2003). The elliptical geometry is inferred from the fact that the anomaly is smaller in the cross-section A–A′ than in cross-section B–B′ (Fig. 4a). The magma chamber is approximated by an ellipsoid with semi-axes lengths of: $a = 11.5$ km, $b = 4.7$ km, and $c = 2.5$ km. The maximum horizontal axis is oriented in the direction of N45.6W. The center of the ellipsoid is assumed to be located at depth of 9 km. Two isothermal surfaces of $T = 520\,^\circ C$ and $T = 300\,^\circ C$ characterizing the solution are shown in Fig. 5. Note that the cupola of the increased temperature merges with the regional isotherm below to produce a diapir-like pattern. Once the 3D temperature field is obtained, the temperature of each 2D slice is easily calculated for the nodes of the 2D unstructured finite-element mesh. Mechanical numerical experiments correspond to the central horizontal section through the ellipsoid using viscosity distributions in accordance with the chosen rheology and the estimated temperature field.

4.2.1. The magma/fault system in transtension

The kinematics scheme used corresponds to GPS data (Hager et al., 2003). To model the fault interaction with the inclusion, the displacement boundary conditions should be specified on the boundaries of the computational domain to outline the moving blocks involved as e.g., in Parsons et al. (2003). The left side of the block, and the part of the lower side close to the left corner, represent the Sierra-Nevada block moving at a constant rate. The right side of the computation domain is fixed. The discontinuity corresponding to the Airport Lake fault starts from the lower side; it penetrates the brittle rocks and reaches the brittle–ductile boundary in the cupola above the intrusion. Its counterpart to the NW, behind the magma chamber, is intentionally excluded to observe the preferred orientation that results from the interaction with the weak inclusion. Again, as it is not possible to introduce gravity loading in 2D sections, only shear stresses are considered. The displacement boundary conditions applied to the left side and part of the lower side near the corner, roughly represent the observed relative motion of the Sierra-Nevada block in NNW direction (N32W) along the Black-Water–Little Lake fault as depicted in Fig. 6.
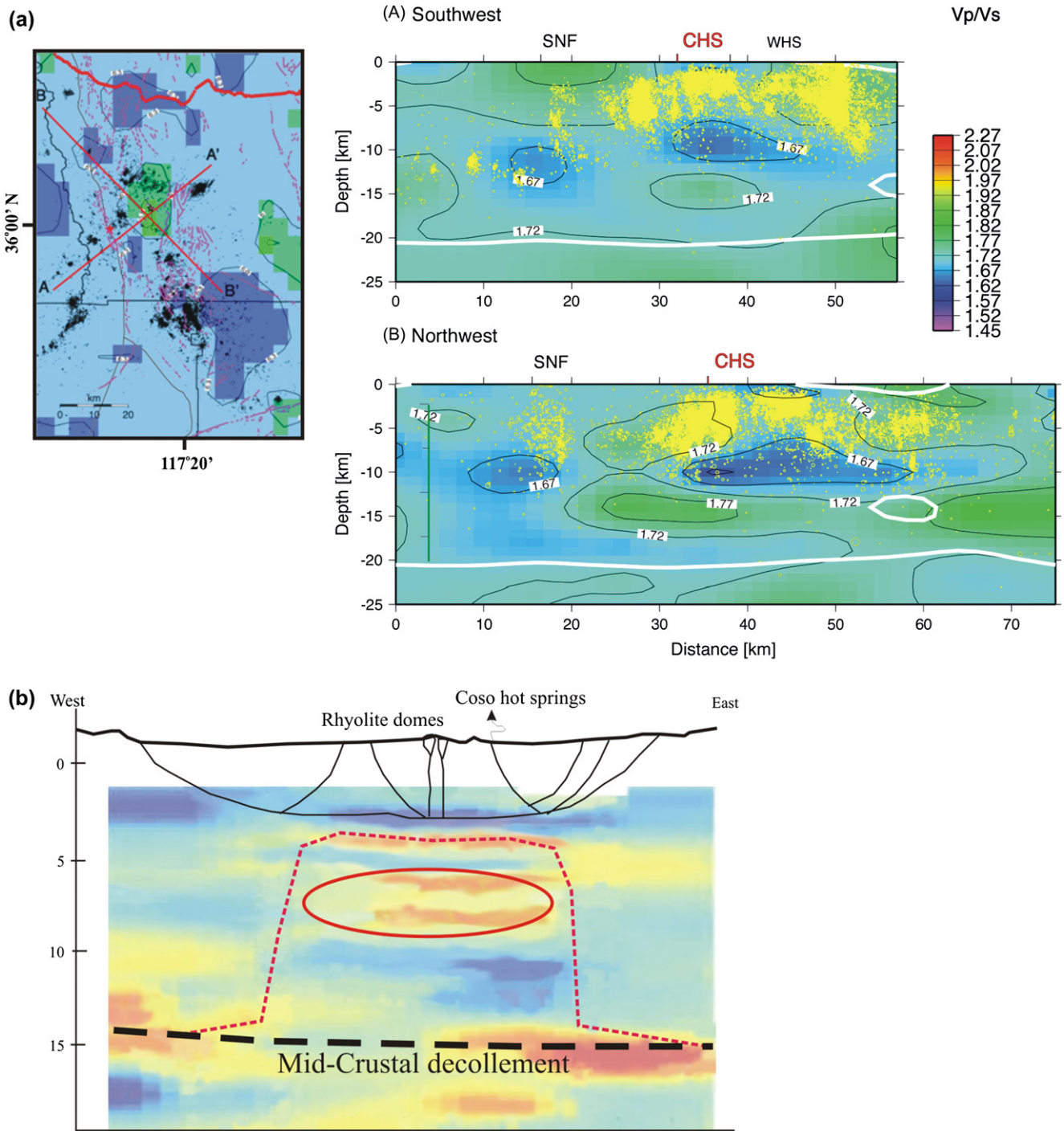
Fig. 4. (a) Seismic structure of the Coso field. Vertical sections of V_p/V_s distributions with superimposed earthquakes epicenters. The position of the profiles is displayed on the map (from Hauksson and Unruh, 2003) (reproduced by permission from U.S. Navy Geothermal Program Office). (b) Teleseismic data from Wilson et al. (2003). The red ellipse approximately corresponds to the position of the assumed magma chamber; red dashes show the possible position of the brittle–ductile transition boundary (modified by permission of American Geophysical Union).

5. Results

The calculations were performed to model a deformation history of about 2000–3000 yrs (sufficient time for strains to accumulate). As shown in Fig. 7, the differential stress distribution ($S_1 - S_2$) calculated for the initial, mainly elastic, stage of the deformation at $t = 300$ yrs has a butterfly pattern similar

to that observed in the analytical model of a hole (under-pressurized magma chamber) in an elastic plate subjected to extension. Note that the expected symmetry in the pattern of stress distribution is distorted due to the inclination of the axis of the ellipse axis relative to the extension direction, the influence of the boundaries of the computational domain, and that of viscous relaxation. The similarity between the
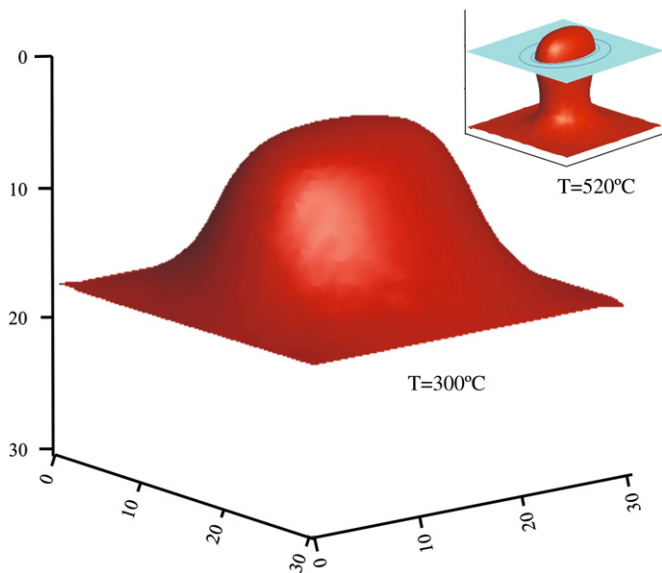
Fig. 5. The 300 and 520 °C isotherms based on 3D calculation of temperature. A cupola of increased temperature (close to the brittle–ductile transition) is evident above the magma body. The isotherm merges with the assumed regional isotherm at a depth of about 28 km. Horizontal cross-sections at the mid-intrusion depth are used for mechanical modeling ($T = 300\,°C$ and $T = 520\,°C$ isotherms indicate the maximum temperature range where brittle–ductile transition is expected to occur).

numerically calculated maximum shear stress, and the observed distribution of epicenters (depth 7–10 km, from Hauksson and Unruh, 2003) in the field can be noted. Large earthquakes at depth are located around the contour of the assumed magma chamber near the maxima of the calculated shear stress intensity. The projection of all earthquakes covers the assumed magma chamber and the zones of maximum shear, while larger earthquakes occur outside the chamber boundary. Only one group (in the SW corner) that apparently has a different origin is located beyond the anticipated zone of the stress concentration in an area around the magma chamber. It should also be noted that, that earthquakes shown are for a limited time interval and one can expect that the distribution of epicenters over a larger time interval would show a better fit. The maximum seismicity at Coso Ridgecrest can be caused by additional factors because a normal fault focal mechanism for some earthquakes is observed there, and also subsidence has been detected in this area.

The results using a stiffer crustal rheology (Koch et al., 1989) better correspond to the observed distribution of deep epicenters around the assumed magma chamber in Coso. A weaker rheology with a viscosity of 8.3×10^{17} Pa s at 750 °C (Jaoul et al., 1984) causes the relaxation of the effective stresses in the thermal aureole and practically extends the chamber boundary to the 400–450 °C isotherm. As a result, there is ambiguity in the chamber parameters; the actual volume of the magma or partially crystallized granite with high exsolved fluid content at a temperature of around 700 °C can be less than the estimate used herein. Probably the seismic data would correspond to the weak area delineated by 400–500 °C isotherm.

The maximum compressive principal stress directions are shown in Fig. 8. There is good agreement between the computed directions and those estimated based on micro-seismicity (Feng and Lees, 1998), and a reconstruction of the compressive principal strain directions (Dewey, 2003). The S_1 directions determined by Feng and Lees (1998) generally are around N12–27E and notably deviate from the calculated directions in the supposed chamber roof. They also found that the S_1 direction in the geothermal field rotates from horizontal to almost vertical in the vertical plane and attributed this to the very fast subsidence rate that is partially caused by reservoir exploitation (vapor extraction and cooling, see e.g., Fialko and Simons, 2000). It should be noted that our model results reflect deep shearing while geophysical measurements are from shallower depths and are also affected by Coso Wash faults system and other processes in the geothermal reservoir.

It is noteworthy that the interpretation of the surface subsidence data by Wicks et al. (2001) indicates a dislocation plane (contraction) that is practically perpendicular to the direction of the extension above the supposed magma chamber. The exact nature of this plane is not certain; however, its orientation resembles a normal fault. It might be a zone of strain localization that is transforming into a normal fault. Unruh et al. (2001) also found seismic discontinuities in the roof with similar parameters that do not manifest themselves on the surface, such as Coso-Wash fault. More detailed comparison can be made using a 3D model based on envisaged factors.

6. Discussion

We have examined the mechanical interaction between an elliptically shaped magma chamber and a fault subject to transtension with reference to the Coso geothermal field. However, the mechanical behavior of such a system is of interest in other geological problems. For example Milano et al. (2004) have modeled stress distribution in the Campanian Plain extension zone (Southern Italy), emphasizing the role of a hydrothermally weakened "inclusion" (40×20 km at a depth of 3 km) in deflecting the principal stress directions and localizing the strongest earthquakes. The authors found that the maximum historical earthquakes in the region occurred in the areas of maximum shear stress.

The distribution of the maximum shear stress for the case of a weak inclusion presented herein, and in Milano et al. (2004), are similar to the δ-shaped zones produced by a stiff inclusion in a shearing viscous matrix (Samanta et al., 2002). Viscous flow around stiff crystal inclusions has been studied in structural geology for their precise and proper application in the kinematic analysis of deformed rocks. An inclusion along with its pair of tails rotates clockwise in dextral shear. Similarly, it can be expected that a strike-slip dextral fault would tend to overstep the magmatic domain in a clock-wise fashion following the maximum shear stress trajectory. This can be seen in Fig. 9, which shows the results of calculation for a longer time ($t = 3000$ yrs) corresponding to the stage of effective viscous relaxation. This is a plausible scenario in the Coso volcano-magmatic center. The geologic setting of the field is
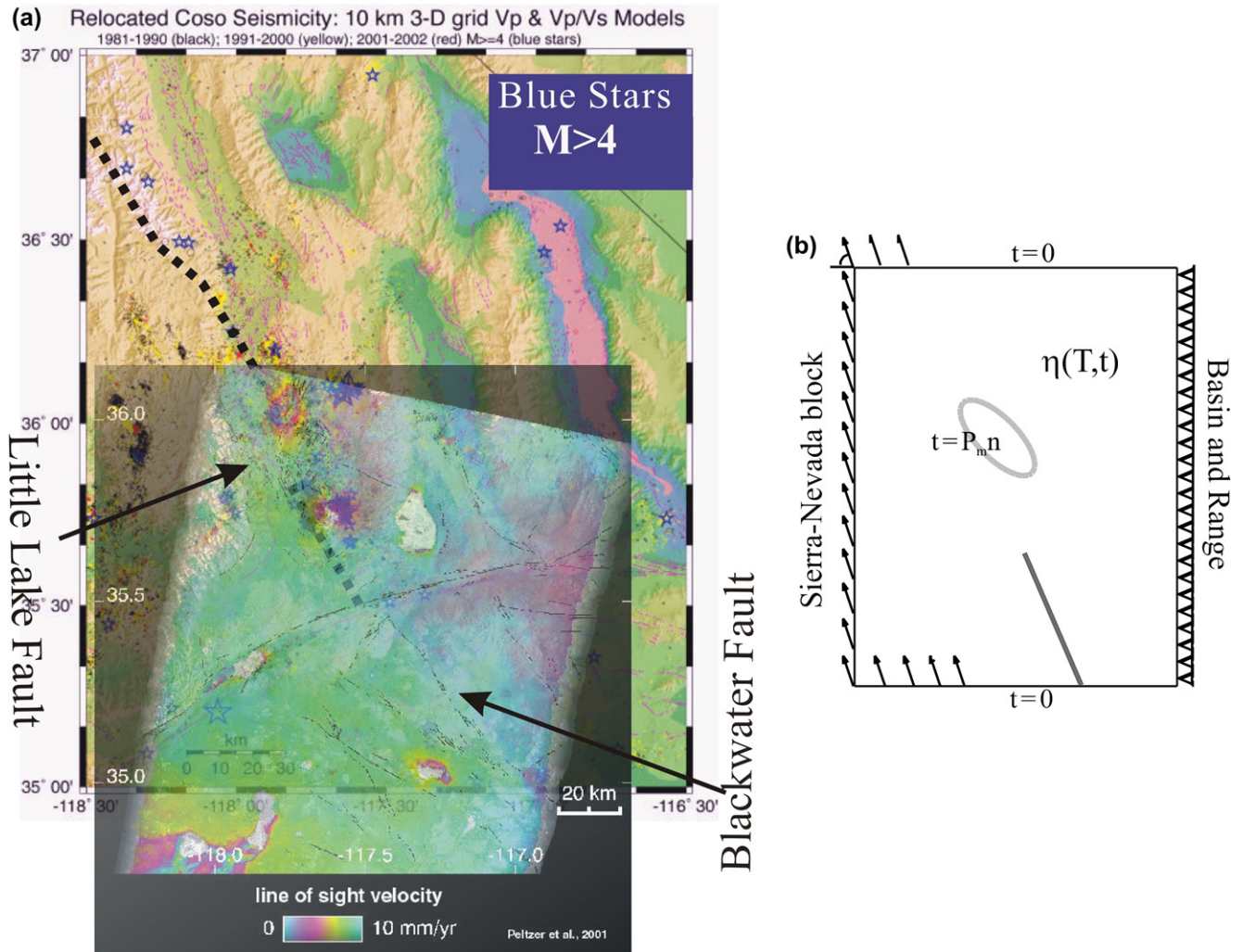
Fig. 6. A horizontal section through Coso: (a) INSAR data from Peltzer et al. (2001) are superimposed on the seismicity section (Hauksson and Unruh, 2003) at the depth 10 km; (b) Boundary conditions used in numerical experiments. Displacements are prescribed on parts of the boundary (inclined arrows). Complimentary parts are stress free; also shown are the fault (red line) and the projection of the position of the elliptical magma body (t, traction, n is the normal).

commonly interpreted as a releasing bend step-over in a dextral strike-slip fault system (Monastero, 2002). In this system, the Airport Lake and Owens Valley Faults are extended along a nearly straight line, so that it is plausible that the structure is the result of a fault overstepping the thermally weakened rocks around the magma body in accordance with the model presented here. This view is consistent with the existence of a seismogenic zone above the brittle–ductile transition zone in the crust and the behavior of the faults as they approach it.

The seismogenic zone is thought to exist above the brittle–ductile transition depth at temperatures below some "cut-off" level. As demonstrated by the large database on California seismicity (Bonner et al., 2003) and the accurate temperature depth profile calculations accounting for the observed heat fluxes, heat generation and conduction, the cut-off temperature for 99% of seismic events is $450 \pm 50\,^{\circ}\mathrm{C}$. This is higher than the frequently referenced temperature of $300 \pm 50\,^{\circ}\mathrm{C}$ for the brittle–ductile transition based on the distinct decrease of permeability (Bailey, 1990; Fournier, 1991). The depth where the temperature reaches $400–500\,^{\circ}\mathrm{C}$ depends on the location, and

is about $15–17$ km around Coso. The brittle–ductile transition zone is also detected as a mid-crustal anisotropic converter with seismic methods (Jones and Phinney, 1998) and is associated with major shear zones extending down from the large normal faults in the region as drawn by Wernicke (1992). A seismic converter has been observed farther to the north and east of Coso and appears to underlie a large part of eastern California (Jones and Phinney, 1998). Due to local heating associated with the long existing Coso silicic magmatic center, this rheological divider rises up to depths of about $4–4.5$ km and is absent at greater depths. It is marked by the listric termination of normal faults in the thermal aureole of the magma chamber (Unruh et al., 2001; Pullammanappallil et al., 2001). Similarly, in horizontal sections like those used in our model a strike-slip fault that propagates in the brittle rocks of the upper crust would bypass the viscous cupola around the Coso magmatic center as described here.

In our simulations, we have used rock viscosities of $\eta = 5.5 \times 10^{19}$ Pa s at $T = 500\,^{\circ}\mathrm{C}$ for the stiff case, and $\eta = 2.0 \times 10^{19}$ Pa s at $T = 500\,^{\circ}\mathrm{C}$ for the weak case, based
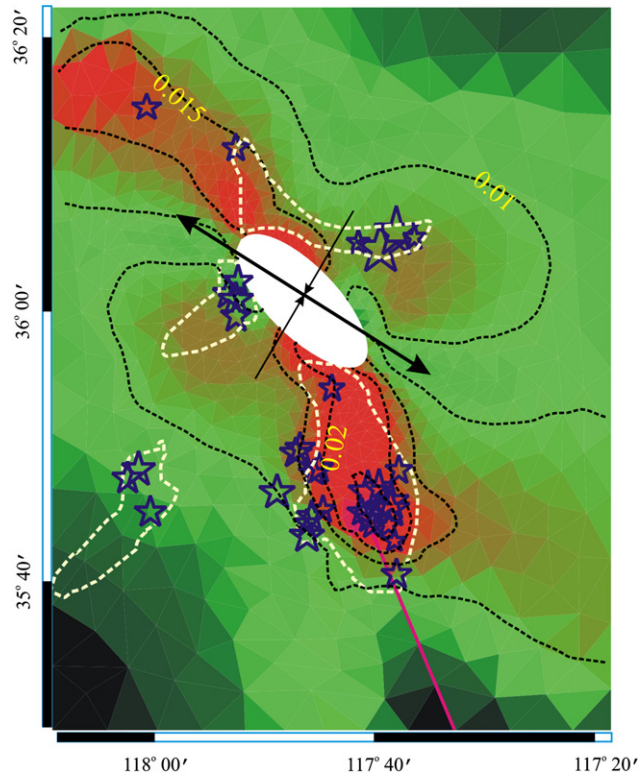
Fig. 7. Distribution of the maximum differential stress ($S_1 - S_2$) accumulated in a short time interval of 300 yrs. Also shown are the relocated Coso seismicities (blue stars) during 1981—1990 at depths of 7—10 km (Hauksson and Unruh, 2003). The purple line depicts the active Airport Lake fault. Black arrows show the principal strain directions in zones away from the magma body.
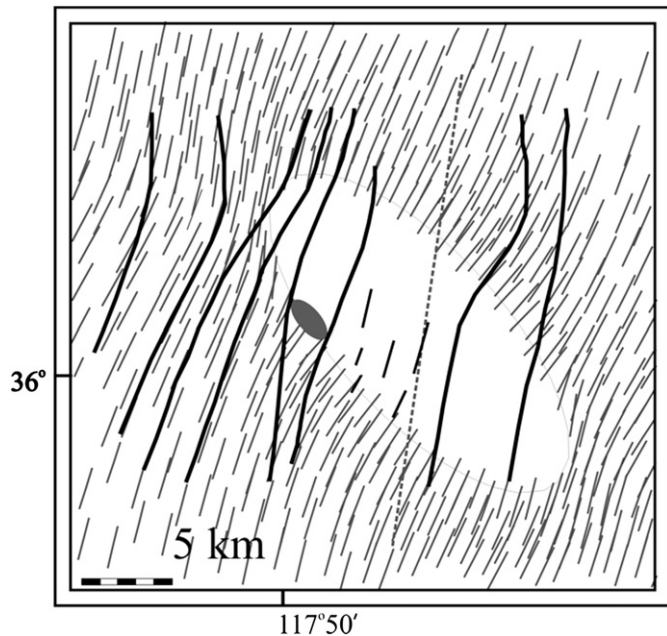

Fig. 9. Calculated maximum shear stress distribution after 2000—3000 yrs. Notice the tendency for the Airport Lake fault to overstep the ''magmatic inclusion'' by following the maximum shear stress zones. The Coso Wash fault intersects the roof of the ''inclusion'' and tends to connect the Owens Valley (OV on the plot) and Airport Lake faults.

on the studies of Koch et al. (1989), and Jaoul et al. (1984). These values are higher than those estimated by Newman et al. (2006) for the thermal aureole of the magma chamber in the Long-Valley system via interpretation of the real-time geodetic and geophysical data. A reason for this is that Newman et al. (2006) interpret the fine structure in the zone of partially crystallized mash rather than the metamorphic rocks in the thermal aureole. It is more consistent to consider viscosity as a function of temperature, as in our study, than to arbitrary place elliptical or spherical shells of fixed viscosities around a magma body (Newman et al., 2006). However, both studies demonstrate that it is essential to account for the lowered viscosity of the thermal aureole when modeling the mechanical response of a magma chamber, its internal pressure variations, and its external deformations. Viscosity depends on many factors such as the presence of fluid, fluid composition and pressure, as well as rock texture, composition and strain rate. A poorly constrained rheology for the surrounding rocks points to uncertainty when solving the inverse problem of finding the position and size of a magma body.

Fig. 8. Trajectories of the major principal stress around the Coso magmatic center at the initial stage of deformation (as in Fig. 7). The short dashes correspond to data from Feng and Lees (1998). The dashed lines are from our calculations. Thick dashed line depicts the position of the Coso Wash fault, and the red lines are the trajectories of the maximum strain directions from Dewey (2003). The small filled ellipse shows the position of Sugar Loaf Mt.
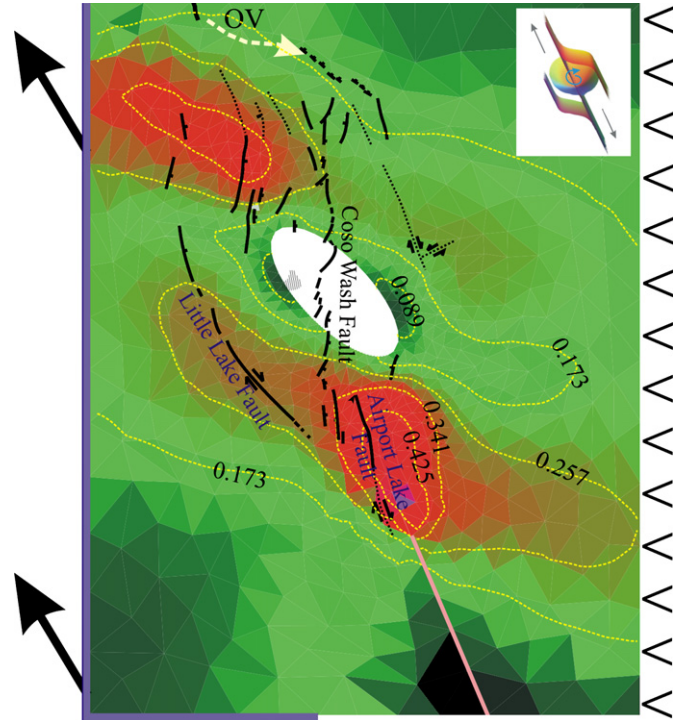
Acknowledgments

References

Bailey, R.C., 1990. Trapping of aqueous fluids in the deep crust. Geophysics Research Letters 17, 1129–1132.

Bonner, J.L., Blackwell, D.D., Herrin, E.T., 2003. Thermal constraints on earthquake depths in California. Bulletin of the Seismological Society of America 93 (N6), 2333–2354, doi:10.1785/0120030041.

Carstensen, C., Scherf, O., Wriggers, P., 1999. Adaptive finite elements for elastic bodies in contact. SIAM Journal Scientific Computing 20, 1605–1626.

Cheng, A.H.-D., Golberg, M.A., Kansa, E.J., Zammito, G., 2003. Exponential convergence and H-c multiquadric collocation method for partial differential equations. Numerical Methods in Partial Differential Equations 19, 571–594.

Combs, J., 1980. Heat flow in the Coso geothermal area, Inyo County, California. Journal of Geophysical Research 85 (B5), 2411–2424.

Corti, G., Bonini, M., Conticelli, S., Innocenti, F., Manetti, P., Sokoutis, D., 2003. Analogue modeling of continental extension: a review focused on the relations between the patterns of deformation and the presence of magma. Earth-Science Reviews 63, 169–247.

Dewey, J.F., 2003. Fault block rotation and strain in transtension. In: Monastero, F. (Ed.), Proceedings of the Eighth Annual Technical Symposium. U.S. Navy Geothermal Program Office, University of CA-Davis (May 29–30).

Feng, Q., Lees, J.M., 1998. Microseismicity, stress, and fracture in the Coso geothermal field, California. Tectonophysics 289, 221–238.

Fialko, Y., Simons, M., 2000. Deformation and seismicity in the Coso geothermal area, Inyo County, California: observations and modeling using satellite radar interferometry. Journal of Geophysical Research 105, 21,781–21,794.

Fournier, R.O., 1991. The transition from hydrostatic to greater than hydrostatic fluid pressure in presently active continental hydrothermal systems in crystalline rock. Geophysical Research Letters 18, 955–958.

Hager, B.H., Hetland, E.A., King, R.W., McClusky, S., Mead, B.J., 2003. Anomalous geodetic displacements and velocity changes associated with the July 17, 2001 Coso Junction earthquake. In: Monastero, F. (Ed.), Proceedings of the Eighth Annual Technical Symposium. U.S. Navy Geothermal Program Office, University of CA-Davis (May 29–30).

Hauksson, E., Unruh, J.R., 2003. Three-dimensional V_p and V_p/V_s velocity models and spatial-temporal seismicity patterns along the intra-continental plate boundary in central-eastern California. In: Monastero, F. (Ed.), Proceedings of the Eighth Annual Technical Symposium. U.S. Navy Geothermal Program Office, University of CA-Davis (May, 29–30).

Jaoul, O., Tullis, J., Kronenberg, A., 1984. The effect of varying water contents on the creep behavior of Heavitree quartzite. Journal of Geophysical Research 89, 4298–4312.

Jones, C.H., Phinney, R.A., 1998. Constraints on the seismic structure of the lithosphere from teleseismic converted arrivals observed at small arrays in the southern Sierra Nevada and vicinity, California. Journal of Geophysical Research 103, 10,065–10,090.

Koch, P.S., Christie, J.M., Ord, A., George Jr., R.P., 1989. Effect of water on the rheology of experimentally deformed quartzite. Journal of Geophysical Research 94, 13,975–13,996.

Manley, C.R., Bacon, C.R., 2000. Rhyolite thermobarometry and the shallowing of the magma reservoir, Coso volcanic field, California. Journal of Petrology 41, 149–174.

Milano, G., Petrazzuoli, S., Ventura, G., 2004. Effects of the hydrothermal circulation on the strain field of the Campanian Plain. Terra Nova 16 (4), 205–209.

Miller, M.M., Johnson, D.J., Dixon, T.H., Dokka, R.K., 2001. Refined kinematics of the eastern California shear zone from GPS observations, 1993–1998. Journal Geophysical Research 106, 2245–2264.

Monastero, F.C., 2002. An overview of industry–military cooperation in the development of power operations at the Coso geothermal field in southern California. Geothermal Resources Council Bulletin 31 (5), 188–194.

Newman, A.V., Dixon, T.H., Gourmelen, N., 2006. A four-dimensional viscoelastic model for deformation of the Long Valley Caldera, California, between 1995 and 2000. Journal of Volcanology and Geothermal Research 150, 244–269.

Parsons, T., Sliter, R., Geist, E.L., Jachens, R.C., Jaffe, B.E., Foxgrover, A., Hart, P.E., McCarthy, J., 2003. Structure and mechanics of the Hayward–Rodgers Creek fault step-over, San Francisco Bay, California. Bulletin Seismological Society of America 93, 2187–2200.

Patane, D., Barberi, G., Cocina, O., De Gori, P., Chiarabba, C., 2006. Time-resolved seismic tomography detects magma intrusions at Mount Etna. Science 313, 821–823.

Peltzer, G., Crampe, F., Hensley, S., Rosen, P., 2001. Transient strain accumulation and fault interaction in the Eastern California shear zone. Geology 29, 975–978.

Pullammanappallil, S., Honjas, W., Unruh, J., 2001. Three-dimensional acoustic velocity analysis of the Coso geothermal field. In: Monastero, F. (Ed.), Proceedings of the Eighth Annual Technical Symposium. U.S. Navy Geothermal Program Office, University of CA-Davis (May 29–30).

Samanta, S.K., Mandal, N., Chakraborty, C., 2002. Development of structures under the influence of heterogeneous flow field around rigid inclusions: insights from theoretical and numerical models. Earth-Science Reviews 58, 85–119.

Savin, G., 1970. Stress Distribution Around Holes. NASA, Washington, D.C..

Schmid, D.W., Podladchikov, Y.Y., 2003. Analytical solutions for deformable elliptical inclusions in general shear. Geophysical Journal International 155, 269–288.

Simakin, A., Ghassemi, A., 2005. Modeling deformation of partially melted rock using a poro-viscoelastic rheology with dynamic power law viscosity. Tectonophysics 397, 195–209.

Stockhert, B., Brix, M., Kleinschrodt, R., Hurford, A.J., Wirth, R., 1999. Thermochronometry and microstructures of quartz-a comparison with experimental flow aws and predictions on the temperature of the brittle-plastic transition. Journal Structural Geology 21, 351–369.

Unruh, J., Pullammanappallil, S., Honjas, W., Monastero, F., 2001. New seismic imaging of the Coso geothermal field, Eastern California. In: Proceedings of the 26th Stanford Geothermal Workshop, January 2001.

Unruh, J., Streig, A., Sundermann S., 2003. Mapping and characterization of neotectonic structures in a releasing stepover, northern Coso Range, eastern California. In: Monastero, F. (Ed.), Proceedings of the Eighth Annual Technical Symposium. U.S. Navy Geothermal Program Office, University of CA-Davis (May 29–30).

Weinberg, R.F., Sial, A.N., Mariano, G., 2004. Close spatial relationship between plutons and shear zones. Geology 32 (5), 377–380.

Welhan, J.A., Poreda, R.J.W., Craig, H., 1988. Helium isotopes in geothermal and volcanic gases of the western US, I. Regional variability and magmatic origin. Journal of Volcanology and Geothermal Research 34, 185–189.

Wernicke, B., 1992. Cenozoic extensional tectonics of the U.S. Cordillera. In: Burchfiel, B.C., Lipman, P.W., Zoback, M.L. (Eds.), The Cordilleran Orogen: Conterminous US. The Geology of North America, vol. G-3. Geological Society of America, Boulder, Colorado, pp. 553–581.

Wicks, C., Thatcher, W., Monastero, F., Hasting, M., 2001. Steady-state deformation of the Coso Range, East-Central California, Inferred from Satellite Radar Interferometry. Journal of Geophysical Research 106, 13769–13780.

Wilson, C.K., Jones, C.H., Gilbert, H.J., 2003. Single-chamber silicic magma system inferred from shear wave discontinuities of the crust and uppermost mantle, Coso geothermal area, California. Journal Geophysical Research 108 (B5), 2226, doi:10.1029/2002JB001798.